Band-Gap Tuning in Ferroelectric Bi 2 FeCrO 6 Double Perovskite Thin Films

A. Quattropani, D. Stoeffler, T. Fix, G. Schmerber, M. Lenertz, G. Versini, J. Rehspringer, A. Slaoui, A. Dinia, S. Colis

Bandgap Tuning in Ferroelectric Bi_2FeCrO_6 Double Perovskite Thin Films

A. Quattropanni,[*,†] D. Stoeffler,[‡] T. Fix,[†] G. Schmerber,[‡] M. Lenertz,[‡] G. Versini,[‡] J.L. Rehspringer,[‡] A. Slaoui,[†] A. Dinia,[‡] and S. Colis[*,‡]

†*ICube laboratory (Université de Strasbourg and CNRS), 23 rue du Loess, BP 20 CR, 67037 Strasbourg Cedex 2, France*

‡*Université de Strasbourg, CNRS, Institut de Physique et Chimie des Matériaux de Strasbourg, UMR 7504 CNRS, 23 rue du Loess, BP 43, F-67034 Strasbourg Cedex 2, France*

E-mail: alessandro.quattropani@etu.unistra.fr; colis@ipcms.unistra.fr

Abstract

We report in this work on the variation of the optical bandgap and structural properties of epitaxial Bi_2FeCrO_6 films grown by pulsed laser deposition on $SrTiO_3(001)$ substrates. It is shown that the bandgap can be tuned by varying the laser repetition rate during deposition which has a strong impact on the Fe/Cr order inside the Bi_2FeCrO_6 double perovskite structure. *Ab initio* band structure calculations unambiguously show that the presence of antisite defects lead to an increase of the gap with about 0.25 eV with respect to the one calculated in the ideal structure. It is also shown that with increasing Fe/Cr disorder the saturation magnetization is strongly reduced along with the difference between the Fe and Cr valences. These results suggest that the bandgap of Bi_2FeCrO_6 can effectively be engineered by modulating the deposition conditions, thus paving the way for applications such as photovoltaic conversion, memory writing and direct CMOS integration.

Introduction

Although silicon is by far the most used semiconductor in nowadays electronic devices, oxide materials are becoming more and more appealing because of their wide variety of properties such as transparency, chemical stability, abundance, low price, reduced toxicity or versatility of the fabrication techniques. Most of the limitations originate from their relative large bandgap, and therefore, doping is systematically required to address different functions. Oxides can thus be used as transparent conductive materials (Sn-doped In_2O_3[1,2]), magnetic semiconductors (transition metal doped ZnO[3,4] or TiO_2[5]), half metallic materials for spintronic applications ($La_{2/3}Sr_{1/3}MnO_3$,[6,7] Sr_2FeMoO_6[8,9]), multiferroic materials ($BiFeO_3$[10]), photon management materials (rare earth doped ZnO,[11,12] SnO_2[13,14] or CeO_2[15])... More recently, oxides were found to have a potential interest for photovoltaic solar cells.[16,17] The main issue related to these oxide materials is their high bandgap which, in order to fit the AM 1.5G solar spectrum, should be lowered to approach that of an ideal absorber in a single

junction solar cell (around 1.1-1.3 eV).[18] One of the most popular oxide absorber is Cu_2O, which has a bandgap of 2.1 eV and a maximum efficiency when integrated in solar cells of 8.1%.[19] More recently, ferroelectric oxides such as Bi_2FeCrO_6 with a bandgap of about 2 eV,[20] $BiFe_{1-x}Mn_xO_3$,[21] Ho-doped $Bi_5Ti_3FeO_{15}$,[22] $BiXO_3$ (with X = Fe, Mg, Zn, Cd, Ca, Sr)[23,24] or $KBiFe_2O_5$ (gap of 1.6 eV)[25] were also reported to be suited for photovoltaic devices. Although less studied because of stability issues, non-oxide ferroelectrics are also reported to be potentially interesting for photovoltaic applications.[26,27] Due to the ferroelectric character of these materials, no p-n junction is needed to separate the charge carriers[28] and photovoltage values much larger than the bandgap are expected.[29,30] Another advantage is that the bandgap (along with other physical properties) can be tuned either by varying the dopant concentration or by changing the concentration of defects.[31,32] As a matter of fact, Nechache *et al*[33] have recently demonstrated the growth of Bi_2FeCrO_6 with variable bandgaps which exhibited conversion efficiencies of 3.3% and 8.1% in single junction and tandem solar cells, respectively. A good understanding of the relationship between the growth conditions, the Fe/Cr ordering in Bi_2FeCrO_6 and the bandgap is therefore mandatory.

In this paper we show a simple method to obtain thin films of Bi_2FeCrO_6 by pulsed laser deposition showing a modulated bandgap between 1.9 and 2.6 eV. This modulation can be easily obtained by varying the laser repetition rate from 1 to 10 Hz during deposition. In order to better understand the effect of structural defects on the bandgap variation, *ab initio* calculations were carried out. While the defected structures (including antisite defects) result in larger bandgap values ranging between 2.50 and 2.55 eV, the bandgap of "perfect" Bi_2FeCrO_6 is found about 2.3 eV. Although this change does not seem important, it is expected to have an essential role on the open circuit voltage of a PV solar cell and therefore on its conversion efficiency.

Experimental details

Epitaxial Bi_2FeCrO_6 films were grown by pulsed laser deposition on $SrTiO_3(001)$ substrates starting from in-house sintered targets and using a KrF excimer laser (248 nm). All samples were grown at 750°C under 10^{-2} mbar O_2 atmosphere. The films were cooled down after deposition at a rate of 5°C/min in the same atmosphere. The laser power was kept at 26 mJ while its repetition rate was varied from 1 to 10 Hz. This is expected to modulate the concentration of defects, notably antisite defects, in the sample. The film thicknesses of the samples deposited between 2 and 10 Hz range between 60 and 98 nm, as determined from the X-ray reflectivity measurements, although the same number of laser pulses were used in each case. The film thickness of the sample deposited at 1 Hz is about 34 nm as the number of the laser pulses was four times smaller than for the rest of the series.

The crystalline structure of the samples was analyzed by X-ray diffraction using a Rigaku SmartLab diffractometer equipped with a monochromatic source delivering a CuKα_1 incident beam (45 kV, 200 mA, 0.154056 nm). X-ray θ-2θ, reflectivity, rocking curves, and ϕ-scans analyzes were performed in order to confirm the epitaxy of the films, check the presence of spurious phases, determine the film thickness, calculate the in- and out-of-plane correlation lengths and estimate the atomic ordering degree.

The magnetic properties were analyzed at room temperature using a MPMS SQUID-VSM (Quantum Design) magnetometer allowing a maximum field of 7 T. The magnetic field was always applied in the film plane along the [100]$SrTiO_3(001)$ direction.

The optical bandgap of the films was determined from spectroscopic ellipsometry measurements performed on a Horiba Uvisel. The dispersion model used was the Adachi new Fourouhi model.[34] The figure of merit related to χ-squared values was always around 0.05.

Structural and optical properties

Bi_2FeCrO_6 presents a double perovskite structure that can be described in the R3 symmetry (a_{rh} = 0.547 nm and α_{rh} = 60.09°). However, this structure can be be fairly approximated with a pseudo-cubic one.[35] The equivalence of the two symmetries can be evidenced in fig. 1a where both the hexagonal and the pseudo-cubic lattices are clearly visible. This pseudo-cubic symmetry explains why the Bi_2FeCrO_6 growth can be performed on four-fold structures such as the one of $SrTiO_3$.

Fig. 1b shows the X-ray diffraction patterns obtained for Bi_2FeCrO_6 films deposited at different laser frequencies. Except the (00l) peaks of the STO substrate, only the (00l) peaks of the Bi_2FeCrO_6 phase are observed. Their close position at the left side of the STO peaks is in agreement with the very close lattice parameters of pseudo-cubic Bi_2FeCrO_6 (0.3930 nm) and STO (0.3906 nm). These patterns also suggests that the films are grown epitaxially with out-of-plane (OP) lattice parameter c of the Bi_2FeCrO_6 pseudo-cubic phase oriented along the normal to the surface of the STO substrate. No secondary phases could be observed in the resolution limit of the X-ray diffraction technique.[36]

The epitaxial growth of Bi_2FeCrO_6 on STO is clearly shown by the ϕ scan measurements recorded on the STO(111) and BFCO(111) peaks (fig. 1c) of a film grown at 2 Hz. The four peaks observed upon rotation of the sample indicates a four-fold symmetry of the Bi_2FeCrO_6 and a cube-on-cube epitaxial relation of BFCO on STO.

In order to have information on the atomic order between Fe and Cr ions inside the Bi_2FeCrO_6 structure, θ-2θ measurements were carried out along the pseudo-cubic [111]BFCO direction (the sample was tilted by 54.7°). Fig. 1d shows the presence of superstructure peaks (SP) at about 19.6° and 61.2° showing a chemical order in BFCO, i.e. an alternate stacking of Fe and Cr planes along the [111] direction. Note however that, although it is widely accepted that ordered double perovskite structures give raise to superstructure peaks,[33] it is also suggested that such peaks can have different origins such as structural modulations (i.e. periodic cationic displacements) that can be found in ferroelectric oxides.[37]

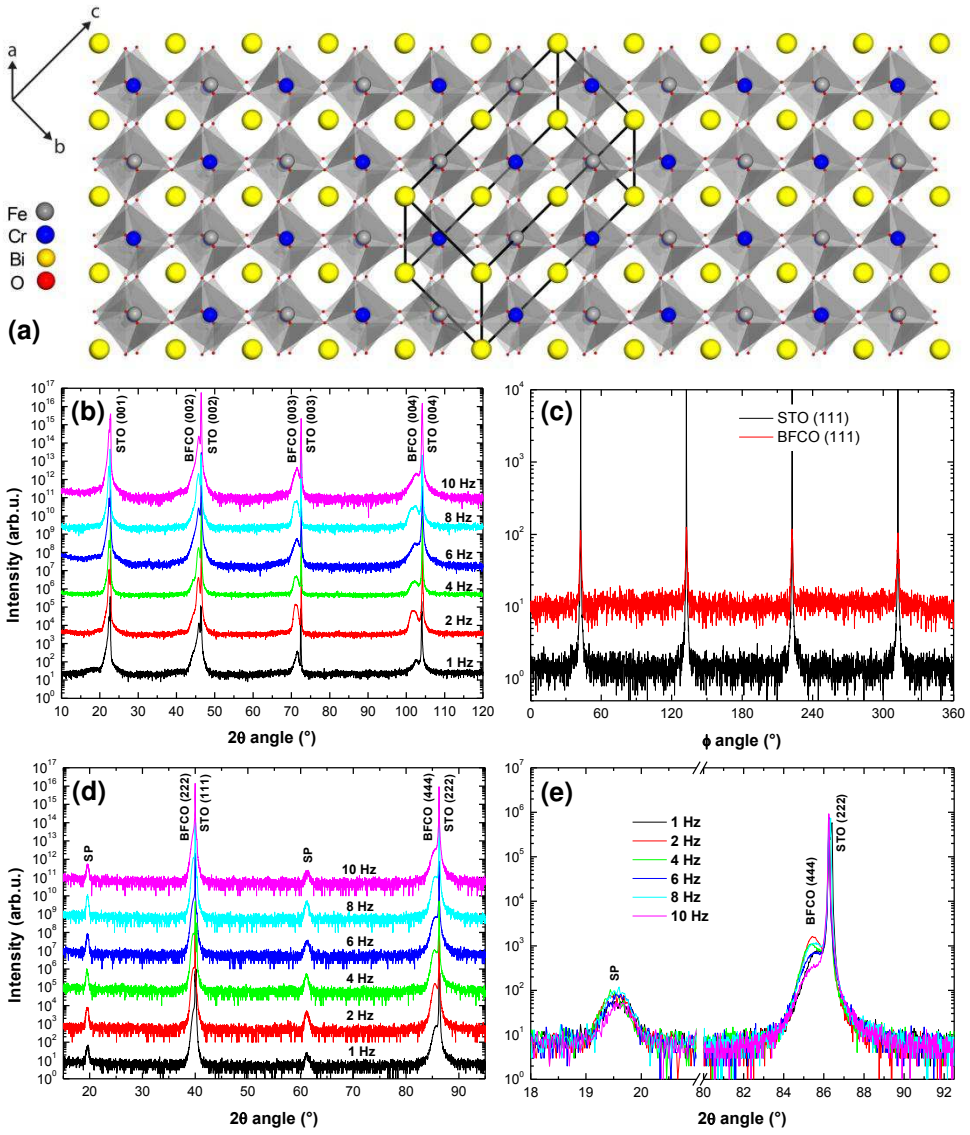

Figure 1: (a) Sketch of the crystalline structure of Bi_2FeCrO_6 (BFCO) showing the equivalency of the pseudo-cubic and hexagonal notations. The hexagonal unit cell and the corresponding axis referential are emphasized with black lines. (b) X-ray diffraction patterns of BFCO thin films deposited on $SrTiO_3$(001) at different laser repetition rates. (c) ϕ scan measurements recorded on the STO(111) and superstructure BFCO(111) peaks showing a four-fold symmetry of the BFCO structure. The diffractogramm recorded on the BFCO peak was shifted along the vertical axis for visibility reasons. (d) X-ray diffraction patterns measured along the pseudo-cubic [111] direction of the Bi_2FeCrO_6 films deposited on $SrTiO_3$(001). (e) Zoom on the superstructure (SP) and BFCO(444) peaks reported in fig. (d). For all figures, the crystalline planes of Bi_2FeCrO_6 have been indexed in the pseudo-cubic structure notation.

The films thickness and the vertical and lateral coherence lengths were obtained from reflectivity (not shown here), θ-2θ (fig. 1b) and rocking curve (not shown here) measurements. Their variation as a function of the laser frequency is reported in fig. 2. Although the same number of laser shots was used for the samples grown from 2 to 10 Hz while the other deposition conditions were identical for all samples, the thickness of the films decreases while increasing the laser frequency. It is also interesting to note that the vertical correlation length (usually known as the crystallite size as calculated using the Debye-Scherrer formula) is much smaller than the thickness and is decreasing while the thickness decreases. This suggests that although epitaxied on the substrate, the Bi_2FeCrO_6 films do not present a columnar growth mode and that a larger concentration of defects is present in the films grown at large laser frequency. This can be easily understood if we keep in mind that the deposition rate of these films is larger. It is also interesting to note that the lateral correlation length is larger on the thinner films. This seems very probably due to the strains induced by the substrate and the progressive relaxation of the BFCO lattice as the film thickness increases. The large correlation values are compatible with the low lattice mismatch between Bi_2FeCrO_6 and the substrate and with the epitaxial character of the films.

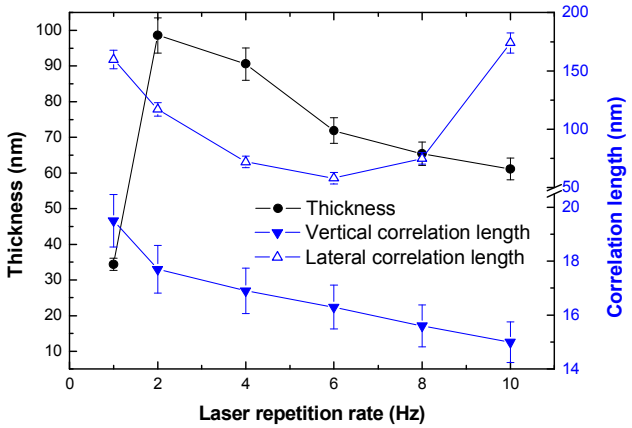

Figure 2: Variation of the films thickness, vertical and lateral correlation lengths as extracted from reflectivity, θ-2θ and rocking curve X-ray diffraction measurements, respectively.

The bandgap for each sample has been extracted by ellipsometry simulations and the results are shown in fig. 3. It is clearly shown that the Bi_2FeCrO_6 film bandgap increases

significantly from 1.9 to 2.6 eV when the deposition rate increases from 1 to 10 Hz, while the crystallite size slightly decreases. One way that possibly explains the bandgap variation is to consider a modification of the bond between the transition metal and the oxygen, altering in this way the hybridization energy and the Coulomb repulsion. It was recently shown that a d^5-d^3 system with both cations in 3+ state (such as Fe and Cr in BFCO[36]), due to homogeneous distribution in the degenerated d orbitals between the two cations, can make a system more rigid[38,39] and less sensitive to strains.[33] Thus, only limited rotation and tilts are possible, which will lead to little changes in the bandgap.[40] Another way to influence the bandgap is to consider the defects existing in the material. One type of defects that is common to double perovskite structures and that can be usually quantified from the XRD data is the antisite defects. Their concentration is proportional to the ratio of the intensities of the superstructure peak (I_{SP}) and of the main peak ($I_{(222)}$ or $I_{(444)}$) of the double perovskite. As in our case the BFCO(222) peak is very close to the $SrTiO_3$(111) one, the BFCO(444) peak was used for a more precise cation ordering estimate. Fig. 3 shows the variation of the $I_{SP}/I_{(444)}$ calculated from fig. 1e (which should be proportional to the Fe/Cr order) as a function of the laser repetition rate. Surprisingly, no clear evolution of the $I_{SP}/I_{(444)}$ ratio is observed with the laser frequency (since the diffractogramms in fig. 1e are very similar). This can be explained on the basis of the work of Shabadi *et al*[37] suggesting that, given the low scattering contrast (close atomic form factors) between the Fe and Cr cations, the presence of the superstructure peak (SP, i.e. BFCO(111)) is not a reliable indicator of the Fe/Cr ordering. This is also supported by the fact that ordering should be very difficult to obtain in Bi_2FeCrO_6. According to different authors, the similar formal valence and ionic radii of Cr^{3+} (0.615 Å) and Fe^{3+} (0.645 Å) ions hampers the chemical order in Bi_2FeCrO_6[33,39] contrary to what is observed in other double perovkistes such as $Sr_2Fe^{3+}Mo^{5+}O_6$[41,42] where the valences are different and the order can be more easily achieved. It can be therefore reasonable to conclude that chemical order in Bi_2FeCrO_6 should be also accompanied by a valence change of Fe and Cr towards a +2 and +4 state, respectively.

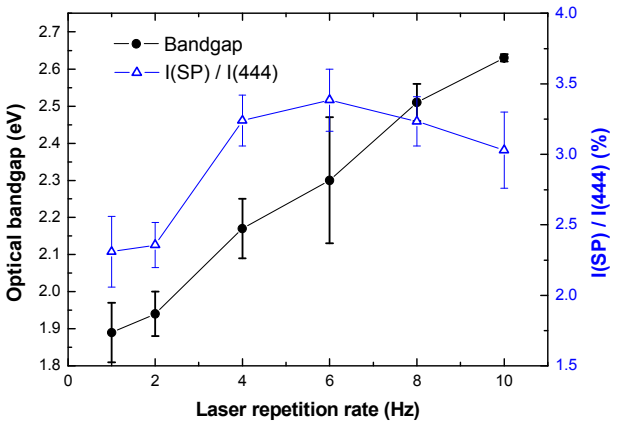

Figure 3: Variation of the films bandgap and order parameter with the laser repetition rate. The bandgap values were extracted from ellipsometry measurements. The order parameter is defined as the intensity ratio of the superstructure (SP) and BFCO(444) peaks reported in fig. 1e.

As X-ray diffraction measurements did not allow to extract information on the Fe/Cr order, it is interesting to look into the magnetic properties of this material. Indeed, the lack of cationic order in Bi_2FeCrO_6 is reported to strongly reduce the saturation magnetization because of antiferromagnetic interactions (Fe-O-Fe and Cr-O-Cr) appearing in the system.[37] Figure 4 shows the room-temperature magnetization loops recorded for Bi_2FeCrO_6 films deposited at a laser repetition rate of 2, 6 and 10 Hz. As observed, the saturation magnetization is small (below 10 emu/cm^3 $\sim$ 0.12 μ_B), much smaller than the values reported in more ordered films (about 150 emu/cm^3).[43] This indicates a strong disorder in our samples that increases with the laser repetition rate.

Our results clearly indicate that a correlation exists between bandgap and atomic disorder, and gives thus the opportunity to engineer the bandgap by controlling the deposition conditions. These variations are also probably correlated to the Fe and Cr valences. In order to have further insight on the correlation between the defect concentration, the bandgap, the saturation magnetization, and the valence of the transition metal ions, *ab initio* calculations have been carried out.

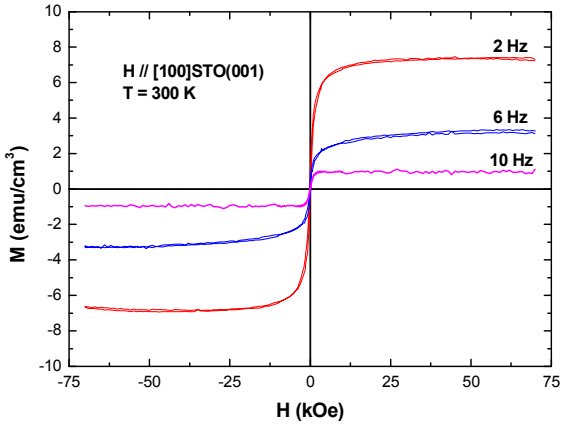

Figure 4: Room-temperature magnetization loops recorded for Bi_2FeCrO_6 films deposited at a laser repetition rate of 2, 6 and 10 Hz.

Ab initio calculations

According to previous investigations,[35,44] we adopted the $R3$ symmetry, corresponding to the space group 146, for the Bi_2FeCrO_6 unit cell. The primitive cell, corresponding to the trigonal representation, contains one Bi_2FeCrO_6 formula unit and is used for full relaxation calculations. The hexagonal representation allows to build a cell containing three Bi_2FeCrO_6 formula units with 3 Fe and 3 Cr sites: this cell is used for simulating chemical configurations with exchanged Fe and Cr atoms and allows to build three new "disordered" configurations.

All calculations were performed using the Vienna Ab initio Simulation Package (VASP5.4)[45,46] allowing to determine accurately the electronic structure and to investigate the magnetic properties of the considered system. It uses so-called Augmented Plane Waves and is based on the Projector Augmented Wave (PAW)[47] method using pseudopotentials to determine the wave function outside the augmentation region. The HSE06 functional[48,49] is used in order to extract the bandgap from the calculation without having to play with empirical parameters like in the GGA+U approach.[50,51] Moreover, we have checked that the bandgap obtained with the HSE06 functional is recovered with the GGA+U method with so large U_{eff} values (around 7 eV) that the electronic structure is strongly distorted. All calculations are performed with a cutoff energy of 400 eV and a k-points sampling of 4×4×4 for the

trigonal cell and of 5×5×2 for the hexagonal cell.

After full relaxation, the lattice parameters and the internal structural position of all atoms were obtained and reported in table 1.

The different hexagonal cells are built keeping these atomic positions unchanged regardless if the Fe or Cr site is occupied by an Fe or a Cr atom. The "perfectly ordered" configuration, where Fe atoms are situated on Fe sites and Cr atoms are situated on Cr sites, presents alternating pure Fe and Cr (0001) planes: we used the notation FCFCFC for this case where the F and C letter corresponds to the Fe and Cr (0001) planes into the stacking. The three different other cases, approximating Fe-Cr chemical disordered configurations, that can be built into the hexagonal cell are then CFFCFC, FFCCFC and FFFCCC. All these structures, with their respective Fe-Cr configurations, are presented in fig. 5.

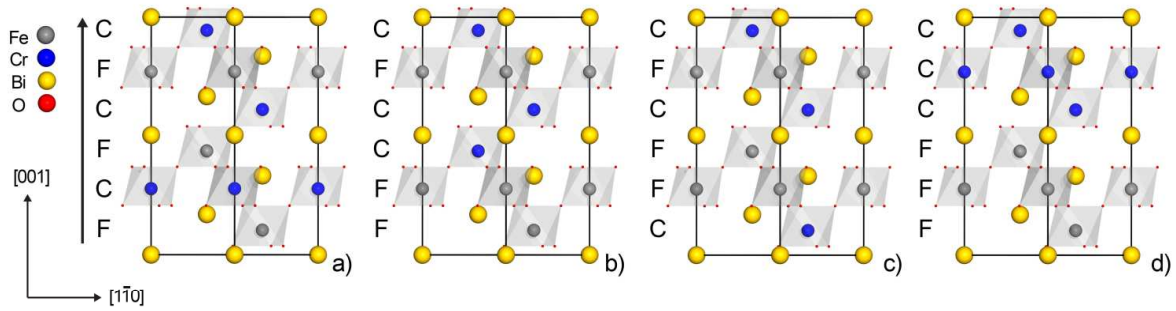

Figure 5: Ideal (a) and disordered (b-d) crystalline structures used for the *ab initio* calculations. The F and C letters accounts for Fe and Cr atomic planes. The black lines represent the hexagonal unit cell.

The total, Fe atoms projected and Cr atoms projected densities of states (DOS) are

Table 1: Structural data (reduced coordinates) of the $R3$ symmetry Bi_2FeCrO_6 trigonal unit cell with a = 0.55135 nm and $\alpha = 59.821°$ obtained from the full relaxation calculation.

Atom	Coordinate	Value
Bi1	(x=y=z)	0
Bi2	(x=y=z)	0.4966
Fe	(x=y=z)	0.2253
Cr	(x=y=z)	0.7194
O1	(x,y,z) (z,x,y) (y,z,x)	(0.4010, 0.5367, 0.9395)
O2	(x,y,z) (z,x,y) (y,z,x)	(0.0353, 0.8938, 0.4419)

displayed in figs. 6 and 7. These DOS present several common features: (i) the occupied Fe states range mainly from -8 to -6.5 eV as a consequence of the strong localisation resulting from the use of the HSE06 functional, (ii) the unoccupied Fe states present a sharp structure around 2.5 eV which determines the bottom of the conduction band, (iii) the Cr occupied states range mainly from -1.5 to 0 eV and are weakly hybridized with the Fe states, (iv) the minority spin energy bandgap is included into the majority spin bandgap. For the "perfectly ordered" configuration, which has the lowest total energy between all four cases, all Fe (respectively Cr) sites being occupied by Fe (Cr) atoms, they carry a positive (negative) magnetic moment of 4.21 μ_B (-2.76 μ_B) giving a total magnetic moment per cell of 6 μ_B (table 2). For the "disordered" configurations, the Fe atom on a Cr site carries a negative magnetic moment and, reciprocally, the Cr atom on a Fe site carries a positive magnetic moment, so that the the total magnetic moment per cell is reduced to 2 μ_B (table 2). The sign of the magnetic moment changes from one magnetic atomic layer to the next one whatever the nature of the magnetic atom is, i.e. only anti-parallel aligned magnetic moments are obtained for neighboring Fe/Fe, Cr/Cr and Fe/Cr atoms. These results strongly support the reduced saturation magnetization observed in our disordered samples. Considering the DOS (figs. 6 and 7), the minority spin band gap $E_g^{\downarrow}$ is entirely included into the majority spin band gap $E_g^{\uparrow}$ so that the band gap for the total DOS is equal to the minority spin band gap. Consequently, the band gap is found equal to 2.30 eV for the "perfectly ordered" configuration whereas it increases to 2.50-2.55 eV (table 2) for the "disordered" configurations in qualitative agreement with the experimental observation. However, the variation of the bandgap remains weak as compared to experiments as a consequence of the weak Fe-Cr hybridization evidenced by the calculations.

This investigation shows also that the used hexagonal cell, which only allows to alter the ordering along the c direction, does not allow considering really different "disordered" configurations and larger cells are required in order to model the "disorder" into planes perpendicular to the c direction. Nevertheless, it is worth noting that these calculations are

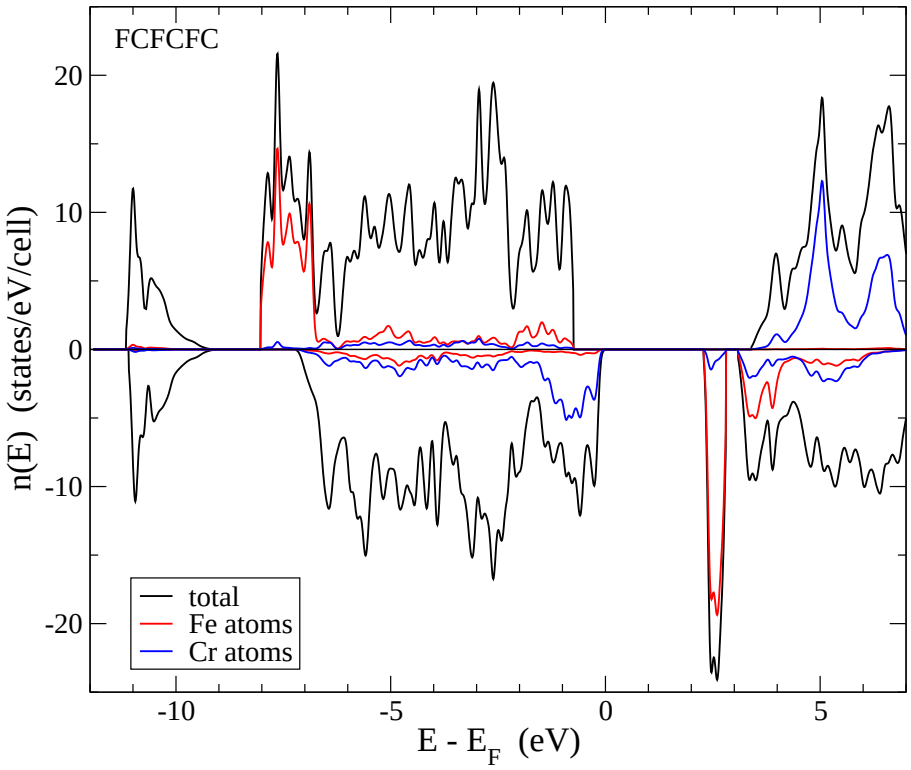

Figure 6: Densities of states (DOS) - total, Fe and Cr atoms projected - for the "perfectly ordered" configuration (FCFCFC) into the hexagonal cell. Positive and negative DOS correspond respectively to majority and minority spins states.

of good support to the experimental results.

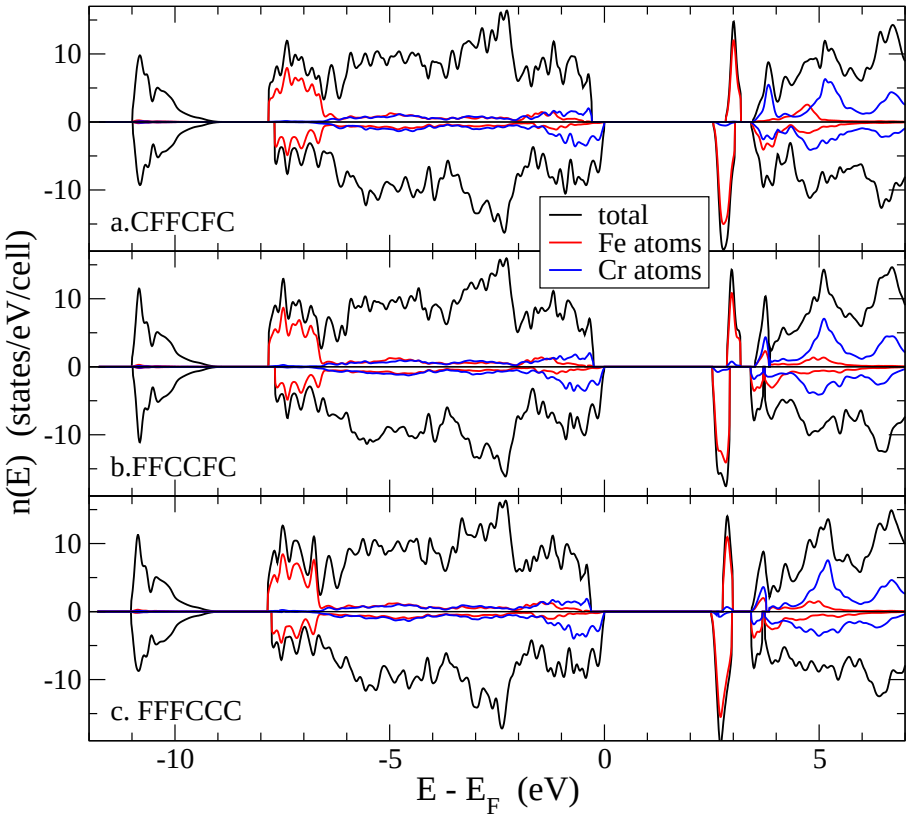

Figure 7: Densities of states (DOS) - total, Fe and Cr atoms projected - for the three "disordered" configurations into the hexagonal cell. Positive and negative DOS correspond respectively to majority and minority spins states.

In order to discuss from a theoretical point of view the relation between the valence of the Fe and Cr atoms and the degree of disorder into the Fe-Cr sequence, we have investigated the charge carried by each atom. First, we have done the so-called Bader charge analysis[52] on the charge densities determined previously using the code developed by Henkelman *et al.*[53–55] We have found that the Bader charges for Fe and Cr are nearly equal (equal to +1.9

Table 2: Local magnetic moments on the 3 Fe and the 3 Cr sites and spin dependent bandgaps for the four configurations considered in this work.

configuration	local magnetic moment (μ_B)	$E_g^{\uparrow}/E_g^{\downarrow}$
FCFCFC	4.212 / -2.760 / 4.212 / -2.760 / 4.212 / -2.760	4.15 / 2.30
FFCCFC	4.212 / -4.168 / 2.807 / -2.762 / 4.175 / -2.804	3.12 / 2.52
CFFCFC	2.864 / -4.126 / 4.164 / -2.805 / 4.176 / -2.808	3.13 / 2.55
FFFCCC	4.212 / -4.167 / 4.163 / -2.807 / 2.823 / -2.762	3.08 / 2.50

$|e|$) and that they do not change when the Fe-Cr sequence is changed. According to a recent similar investigation on Fe_3O_4 and $CaFeO_3$ systems,[56] we conclude that the Bader charge analysis is not very helpful for investigating theoretically the charge ordering in such oxide.

In their work, Wang *et al*[56] demonstrate that charge ordering can be quantitatively investigated by analyzing the Born effective charge (BEC) carried by each atom. Moreover, the BEC determination results from the calculation of the variation of the polarization, which is a global quantity given by integration over the whole cell, and is consequently not sensitive to a defined volume (like a sphere or the Bader analysis volume) around the considered atom. The calculation of the BEC using the HSE06 functional being too much computer time consuming, we have determined the electronic structure with the GGA+U approximation taking $U_{eff} = 4$ eV. We have checked that, by comparing to the results obtained with the HSE06 functional, the GGA+U with $U_{eff} = 4$ eV method describes accurately the occupied states, and consequently the charge density, even if the bandgap is found around 0.7 eV smaller (i.e. about 1.6 eV). This is motivated by the fact that the polarization and the Born effective charges are obtained by summing over the occupied states. The BEC are obtained using the linear-response approach as implemented into VASP[57] and the polarization is calculated into the framework of the modern theory of polarization.[58]

Table 3: Born effective charges Q^*_{zz} on the Fe and Cr atoms for the four cases considered in this work; the variation ΔQ^*_{zz} being calculated relative to the same atom into the "perfectly ordered" FCFCFC configuration. All quantities are given in absolute value of the electron charge $|e|$.

FCFCFC	Fe	Cr	Fe	Cr	Fe	Cr
Q^*_{zz}	+3.86	+3.06	+3.86	+3.06	+3.86	+3.06
FFCCFC	Fe	Fe	Cr	Cr	Fe	Cr
Q^*_{zz}	+3.67	+3.66	+3.49	+3.21	+3.81	+3.07
ΔQ^*_{zz}	-0.19	-0.20	+0.43	+0.15	-0.05	+0.01
CFFCFC	Cr	Fe	Fe	Cr	Fe	Cr
Q^*_{zz}	+3.32	+3.77	+3.64	+3.10	+3.84	+3.31
ΔQ^*_{zz}	+0.26	-0.09	-0.22	+0.04	-0.02	+0.25
FFFCCC	Fe	Fe	Fe	Cr	Cr	Cr
Q^*_{zz}	+3.68	+3.53	+3.69	+3.31	+3.46	+3.20
ΔQ^*_{zz}	-0.18	-0.33	-0.17	+0.25	+0.40	+0.14

Table 3 gives the BEC obtained on each Fe and Cr atom for the four cases considered in the present work. For the "perfectly ordered" configuration, the Fe BEC are found 0.80 $|e|$ larger than the Cr ones in clear contrast to the result obtained by the Bader charge analysis. For the three "disordered" configurations, depending on the Fe-Cr sequence, the BEC show significant variations ΔQ^*_{zz} :

1. for Fe atoms into a Cr-Fe-Cr stacking, ΔQ^*_{zz} are found equal to -0.05 and -0.02 $|e|$ and for Cr atoms into a Fe-Cr-Fe stacking they are found equal to +0.01 and +0.04 $|e|$,

2. for Fe atoms into a Fe-Fe-Cr or Cr-Fe-Fe stacking, ΔQ^*_{zz} are found equal to -0.19, -0.20, -0.09, -0.22, -0.18 and -0.17 $|e|$ and for Cr atoms into a Cr-Cr-Fe or Cr-Cr-Fe stacking they are found equal to +0.43, +0.15, +0.25, +0.26, +0.25 and +0.14 $|e|$,

3. finally, for the Fe atom into a Fe-Fe-Fe stacking, ΔQ^*_{zz} = -0.33 $|e|$ and for the Cr atom into a Cr-Cr-Cr stacking, ΔQ^*_{zz} = +0.40 $|e|$.

This shows clearly that the BEC difference between the Fe and Cr ions is directly related to the level of local Fe-Cr "disorder" varying from 0.57 $|e|$ to 0.15 $|e|$ for a limited "disorder" and being equal to 0.07 $|e|$ for the extreme FFFCCC case. These BEC variations have no impact on the polarization found equal to 57 μC/cm^2 for all considered cases. It can be therefore concluded that, for this system, the higher the Fe-Cr "disorder" is, the smaller the difference between the Fe and Cr BEC is and the lower the energetical stability of the structure is. This result clearly shows a correlation between the chemical order in Bi_2FeCrO_6 and the valence difference between the Fe and Cr ions.

Conclusion

In this work, the structural and optical properties of epitaxial single phase Bi_2FeCrO_6 films of different thickness grown by pulsed laser deposition on $SrTiO_3$(001) substrates are reported. The main result is that the bandgap and the Fe/Cr order of the films can be tuned by varying the laser repetition rate. It is shown that chemically ordered Bi_2FeCrO_6 films have a low

bandgap of about 1.9 eV while in a disordered film this value can reach 2.6 eV. *Ab initio* band structure calculations confirmed indeed the increase of the bandgap in the disordered state, accompanied by a reduction of the saturation magnetization. It is also shown that the existence of the ordered state in Bi_2FeCrO_6 is correlated to the existence of a large valence difference between Fe and Cr. These experimental and theoretical results finally suggest that the Bi_2FeCrO_6 double perovskite films can effectively be engineered to obtain a desired bandgap by controlling the deposition conditions, which can open the path to several applications including photovoltaic conversion, memory writing and direct CMOS integration.

Acknowledgement

This work was carried out under the framework of the FERROPV project supported by the French Agence Nationale de la Recherche (ANR) under the reference ANR-16-CE05-0002-01.

References

(1) Jouane, Y.; Colis, S.; Schmerber, G.; Leuvrey, C.; Dinia, A.; Lévêque, P.; Heiser, T.; Chapuis, Y. A. Annealing treatment for restoring and controlling the interface morphology of organic photovoltaic cells with interfacial sputtered ZnO films on P3HT: PCBM active layers. *J. Mater. Chem.* **2012**, *22*, 1606-1612.

(2) Jouane, Y.; Colis, S.; Schmerber, G.; Dinia, A.; Lévêque, P.; Heiser, T.; Chapuis, Y. A. Influence of flexible substrates on inverted organic solar cells using sputtered ZnO as cathode interfacial layer. *Organic Electronics* **2013**, *14*, 1861-1868.

(3) Belghazi, Y.; Stoeffler, D.; Colis, S.; Schmerber, G.; Ulhaq-Bouillet, C.; Rehspringer, J. L.; Berrada, A.; Aubriet, H.; Petersen, J.; Becker, C.; Ruch, D.; Dinia, A. Magnetic

properties of Al-doped $Zn_{0.95}Co_{0.05}O$ films: Experiment and theory. *J. Appl. Phys.* **2009**, *105*, 113904.

(4) Chang, G. S.; Kurmaev, E. Z.; Boukhvalov, D. W.; Finkelstein, L. D.; Colis, S.; Pedersen, T. M.; Moewes, A.; Dinia, A. Effect of Co and O defects on the magnetism in Co-doped ZnO: Experiment and theory. *Phys. Rev. B* **2007**, *75*, 195215.

(5) Matsumoto, Y.; Murakami, M.; Shono, T.; Hasegawa, T.; Fukumura, T.; Kawasaki, M.; Ahmet, P.; Chikyow, T.; Koshihara, S.; Koinuma, H. Room-temperature ferromagnetism in transparent transition metal-doped titanium dioxide. *Science* **2001**, *291* 854-856.

(6) Bowen, M.; Bibes, M.; Barthélémy, A.; Contour, J. P.; Anane, A.; Lemaître, Y.; Fert, A. Nearly total spin polarization in $La_{2/3}Sr_{1/3}MnO_3$ from tunneling experiments. *Appl. Phys. Lett.* **2003**, *82*, 233-235.

(7) Moubah, R.; Colis, S.; Versini, G.; Barre, S.; Ulhaq-Bouillet, C.; Dinia, A. Structural and magnetic properties of $La_{2/3}Sr_{1/3}MnO_3/SrTiO_3/CoFe_2$ hard-soft magnetic systems. *J. Supercond. Nov. Magn.* **2017**, *30*, 1171-1175.

(8) Serrate, D.; De Teresa, J. M.; Ibarra, M. R. Double perovskites with ferromagnetism above room temperature. *J. Phys.: Condens. Matter* **2007**, *19*, 023201.

(9) Fix, T.; Ulhaq-Bouillet, C.; Colis, S.; Dinia, A.; Bertoni, G.; Verbeeck, J.; Van Tendeloo, G. Nanoscale analysis of interfaces in a metal/oxide/oxide trilayer obtained by pulsed laser deposition. *Appl. Phys. Lett.* **2007**, *91*, 023106.

(10) Wang, J.; Neaton, J. B.; Zheng, H.; Nagarajan, V.; Ogale, S. B.; Liu, B.; Viehland, D.; Vaithyanathan, V.; Schlom, D. G.; Waghmare, U. V.; Spaldin, N. A.; Rabe, K. M.; Wuttig, M.; Ramesh, R. Epitaxial $BiFeO_3$ multiferroic thin film heterostructures. *Science* **2003**, *299*, 1719-1722.

(11) Balestrieri, M.; Ferblantier, G.; Colis, S.; Schmerber, G.; Ulhaq-Bouillet, C.; Muller, D.; Slaoui, A.; Dinia, A. Structural and optical properties of Yb-doped ZnO films deposited by magnetron reactive sputtering for photon conversion. *Solar Energy Materials & Solar Cells* **2013**, *117*, 363-371.

(12) Balestrieri, M.; Colis, S.; Gallart, M.; Ferblantier, G.; Muller, D.; Gilliot, P.; Bazylewski, P.; Chang, G. S.; Slaoui, A.; Dinia, A. Efficient energy transfer from ZnO to Nd^{3+} ions in Nd-doped ZnO films deposited by magnetron reactive sputtering. *J. Mater. Chem. C* **2014**, *2*, 9182-9188.

(13) Bouras, K.; Rehspringer, J.-L.; Schmerber, G.; Rinnert, H.; Colis, S.; Ferblantier, G.; Balestrieri, M.; Ihiawakrim, D.; Dinia, A.; Slaoui, A. Optical and structural properties of Nd doped SnO_2 powder fabricated by the sol-gel method. *J. Mater. Chem. C* **2014**, *2*, 8235-8243.

(14) Bouras, K.; Schmerber, G.; Rinnert, H.; Aureau, D.; Park, H.; Ferblantier, G.; Colis, S.; Fix, T.; Park, C.; Kim, W. K.; Dinia, A.; Slaoui, A. Structural, optical and electrical properties of Nd-doped SnO_2 thin films fabricated by reactive magnetron sputtering for solar cell devices. *Solar Energy Materials & Solar Cells* **2014**, *145*, 134-141.

(15) Balestrieri, M.; Colis, S.; Gallart, M.; Schmerber, G.; Bazylewski, P.; Chang, G. S.; Ziegler, M.; Gilliot, P.; Slaoui, A.; Dinia, A. Photon management properties of rare-earth (Nd,Yb,Sm)-doped CeO_2 films prepared by pulsed laser deposition. *Phys. Chem. Chem. Phys.* **2016**, *18*, 2527-2534.

(16) Ji, W.; Yao, K.; Liang, Y. C. Bulk photovoltaic effect at visible wavelength in epitaxial ferroelectric $BiFeO_3$ thin films. *Adv. Mater.* **2010**, *22*, 1763-1766.

(17) Grinberg, I.; West, D. V.; Torres, M.; Gou, G.; Stein, D. M.; Wu, L.; Chen, G.; Gallo, E. M.; Akbashev, A. R.; Davies, P. K.; Spanier, J. E.; Rappe, A. M. Perovskite oxides

for visible-light-absorbing ferroelectric and photovoltaic materials. *Nature* **2013**, *503*, 509-512.

(18) Shockley W.; Queisser, H. J. Detailed balance limit of efficiency of p-n junction solar cells. *J. Appl. Phys.* **1961**, *32*, 510-519.

(19) Minami, T.; Nishi, Y.; Miyata, T. Efficiency enhancement using a $Zn_{1-x}Ge_x$-O thin film as an n-type window layer in Cu_2O-based heterojunction solar cells. *Appl. Phys. Express* **2016**, *9*, 052301.

(20) Nechache, R.; Harnagea, C.; Licoccia, S.; Traversa, E.; Ruediger, A.; Pignolet, A.; Rosei, F. Photovoltaic properties of Bi_2FeCrO_6 epitaxial thin films. *Appl. Phys. Lett.* **2011**, *98*, 202902.

(21) Xu, X. S.; Ihlefeld, J. F.; Lee, J. H.; Ezekoye, O. K.; Vlahos, E.; Ramesh, R.; Gopalan, V.; Pan, X. Q.; Schlom, D. G.; Musfeldt, J. L. Tunable band gap in $Bi(Fe_{1-x}Mn_x)O_3$ films. *Appl. Phys. Lett.* **2010**, *96*, 192901.

(22) Bai, Y.; Chen, J.; Wu, X.; Zhao, S. Photovoltaic behaviors regulated by band-gap and bipolar electrical cycling in Holmium-doped $Bi_5Ti_3FeO_{15}$ ferroelectric films. *J. Phys. Chem. C* **2016**, *120*, 24637-24645.

(23) Yang, S. Y.; Martin, L. W.; Byrnes, S. J.; Conry, T. E.; Basu, S. R.; Paran, D.; Reichertz, L.; Ihlefeld, J.; Adamo, C.; Melville, A.; Chu, Y.-H.; Yang, C.-H.; Musfeldt, J. L.; Schlom, D. G.; Ager III, J. W.; Ramesh, R. Photovoltaic effects in $BiFeO_3$. *Appl. Phys. Lett.* **2009**, *95*, 062909.

(24) He, J.; Franchini, C.; Rondinelli, J. M. Ferroelectric oxides with strong visible-light absorption from charge ordering. *Chem. Mater.* **2017**, *29*, 2445-2451.

(25) Zhang, G.; Wu, H.; Li, G.; Huang, Q.; Yang, C.; Huang, F.; Liao, F.; Lin, J. New high

T_C multiferroics $KBiFe_2O_5$ with narrow band gap and promising photovoltaic effect. *Sci. Rep.* **2013**, *3*, 1265.

(26) Wang, H.; Gou, G.; Li, J. Ruddlesden-Popper perovskite sulfides $A_3B_2S_7$: A new family of ferroelectric photovoltaic materials for the visible spectrum. *Nano Energy* **2016**, *22*, 507-513.

(27) Bi, F.; Markov, S.; Wang, R.; Kwok, Y. H.; Zhou, W.; Liu, L.; Zheng, X.; Chen, G. H.; Yam, C. Y. Enhanced photovoltaic properties induced by ferroelectric domain structures in organometallic halide perovskites. *J. Phys. Chem. C* **2017**, *121*, 11151-11158.

(28) Kirchartz, T.; Bisquert, J.; Mora-Sero, I.; Garcia-Belmonte, G. Classification of solar cells according to mechanisms of charge separation and charge collection. *Phys. Chem. Chem. Phys.* **2015**, *17*, 4007-4014.

(29) Yuan, Y.; Xiao, Z.; Yang, B.; Huang, J. Arising applications of ferroelectric materials in photovoltaic devices. *J. Mater. Chem. A* **2014**, *2*, 6027-6041.

(30) Yang, S. Y.; Seidel, J.; Byrnes, S. J.; Shafer, P.; Yang, C.-H.; Rossell, M. D.; Yu, P.; Chu, Y.-H.; Scott, J. F.; Ager III, J. W.; Martin, L. W.; Ramesh, R. Above-bandgap voltages from ferroelectric photovoltaic devices. *Nature Nanotech.* **2010**, *5*, 143-147.

(31) Colis, S.; Stoeffler, D.; Mény, C.; Fix, T.; Leuvrey, C.; Pourroy, G.; Dinia, A.; Panissod, P. Structural defects in Sr_2FeMoO_6 double perovskite: Experimental versus theoretical approach. *J. Appl. Phys.* **2005**, *98*, 033905.

(32) Stoeffler, D.; Colis, S. Ab initio study of the electronic structure of Sr_2FeMoO_6 double perovskites presenting oxygen vacancies or/and antisite imperfections. *Mater. Sci. Eng. B* **2006**, *126* 133-138.

(33) Nechache, R.; Harnagea, C.; Li, S.; Cardenas, L.; Huang, W.; Chakrabartty, J.; Rosei, F. Bandgap tuning of multiferroic oxide solar cells. *Nature Photonics* **2014**, *9*, 61-67.

(34) Yoshikawa H.; Adachi, S. Optical constants of ZnO. *Jpn. J. Appl. Phys.* **1997**, *36*, 6237-6243.

(35) Baettig, P.; Ederer, C.; Spaldin, N. A. First principles study of the multiferroics $BiFeO_3$, Bi_2FeCrO_6, and $BiCrO_3$: Structure, polarization, and magnetic ordering. *Phys. Rev. B* **2005**, *72*, 214105.

(36) Nechache, R.; Harnagea, C.; Carignan, L. P.; Gautreau, O.; Pintilie, L.; Singh, M. P.; Ménard, D.; Fournier, P.; Alexe, M.; Pignolet, A. Epitaxial thin films of the multiferroic double perovskite Bi_2FeCrO_6 grown on (100)-oriented $SrTiO_3$ substrates: Growth, characterization, and optimization. *J. Appl. Phys.* **2009**, *105*, 061621.

(37) Shabadi, V.; Major, M.; Komissinskiy, P.; Vafaee, M.; Radetinac, A.; Baghaie Yazdi, M.; Donner, W.; Alff, L. Origin of superstructures in (double) perovskite thin films. *J. Appl. Phys.* **2014**, *116*, 114901.

(38) Vailionis, A.; Boschker, H.; Siemons, W.; Houwman, E. P.; Blank, D. H. A.; Rijnders, G.; Koster, G. Misfit strain accommodation in epitaxial ABO_3 perovskites: Lattice rotations and lattice modulations. *Phys. Rev. B* **2011**, *83*, 064101.

(39) Ohtomo, A.; Chakraverty, S.; Mashiko, H.; Oshima, T.; Kawasaki, M. Spontaneous atomic ordering and magnetism in epitaxially stabilized double perovskites. *J. Mater. Res.* **2013**, *28*, 689-695.

(40) Rondinelli, J. M.; Spaldin, N. A. Substrate coherency driven octahedral rotations in perovskite oxide films. *Phys. Rev. B* **2010**, *82*, 113402.

(41) Kobayashi, K.-I.; Kimura, T.; Sawada, H.; Terakura, K.; Tokura, Y. Room-temperature

magnetoresistance in an oxide material with an ordered double-perovskite structure. *Nature* **1998**, *395*, 677-680.

(42) Anderson, M. T.; Greenwood, K. B.; Taylor, G. A.; Poeppelmeier, K. R. B-cation arrangements in double perovskites. *Prog. Solid State Chem.* **1993**, *22*, 197-233.

(43) Nechache, R.; Harnagea, C.; Pignolet, A. Multiferroic properties-structure relationships in epitaxial Bi_2FeCrO_6 thin films: recent developments. *J. Phys.: Condens. Matter* **2012**, *24*, 096001.

(44) Zhe-Wen, S.; Bang-Gui, L. Electronic structure and magnetic and optical properties of double perovskite Bi_2FeCrO_6 from first-principles investigation. *Chin. Phys. B* **2013**, *22*, 047506.

(45) Kresse, G.; Furthmüller, J. Efficient iterative schemes for ab initio total-energy calculations using a plane-wave basis set. *Phys. Rev. B* **1996**, *54*, 11169-11186.

(46) Kresse, G.; Joubert, D. From ultrasoft pseudopotentials to the projector augmented-wave method. *Phys. Rev. B* **1999**, *59*, 1758-1775.

(47) Blöchl, P. E. Projector augmented-wave method. *Phys. Rev. B* **1994**, *50*, 17953-17979.

(48) Heyd, J.; Scuseria, G. E.; Ernzerhof, M. Hybrid functionals based on a screened Coulomb potential. *J. Chem. Phys.* **2003**, *118*, 8207-8215.

(49) Krukau, A. V.; Vydrov, O. A.; Izmaylov, A. F.; Scuseria, G. E. Influence of the exchange screening parameter on the performance of screened hybrid functionals. *J. Chem. Phys.* **2006**, *125*, 224106.

(50) Perdew, J. P.; Burke, K.; Ernzerhof, M. Generalized gradient approximation made simple. *Phys. Rev. Lett.* **1996**, *77*, 3865-3868.

(51) Dudarev, S. L.; Botton, G. A.; Savrasov, S. Y.; Humphreys, C. J.; Sutton, A. P. Electron-energy-loss spectra and the structural stability of nickel oxide: An LSDA+U study. *Phys. Rev. B* **1998**, *57*, 1505-1509.

(52) Bader, R. F. W. *Atoms in Molecules - A quantum theory*; Oxford University Press, New York, 1990.

(53) Henkelman, G.; Arnaldsson, A.; Jonsson, H. A fast and robust algorithm for Bader decomposition of charge density. *Comput. Mater. Sci.* **2006**, *36*, 354-360.

(54) Sanville, E.; Kenny, S. D.; Smith, R.; Henkelman, G. Improved grid-based algorithm for Bader charge allocation. *J. Comp. Chem.* **2007**, *28*, 899-908.

(55) Tang, W.; Sanville, E.; Henkelman, G. A grid-based Bader analysis algorithm without lattice bias. *J. Phys.: Condens. Matter* **2009**, *21*, 084204.

(56) Wang, Y.; Lee, S. H.; Zhang, L. A.; Shang, S. L.; Chen, L.-Q.; Derecskei-Kovacs, A.; Liu, Z.-K. Quantifying charge ordering by density functional theory: Fe_3O_4 and $CaFeO_3$. *Chem. Phys. Lett.* **2014**, *607*, 81-84.

(57) Gajdoš, M.; Hummer, K.; Kresse, G.; Furthmüller, J.; Bechstedt, F. Linear optical properties in the projector-augmented wave methodology. *Phys. Rev. B* **2006**, *73*, 045112.

(58) Resta, R. Modern theory of polarization in ferroelectrics. *Ferroelectrics* **1994**, *151*, 49-58.

Graphical TOC Entry